Iceland Kinematics from InSAR

Yunmeng Cao[1,2], Sigurjón Jónsson[1], Sigrún Hreinsdóttir[2]

[1]King Abdullah University of Science and Technology (KAUST), Thuwal 23955, Saudi Arabia, [2]Now at GNS Science, Lower Hutt, New Zealand

Key points:

- Time-series of countrywide displacements over Iceland from 2015 to 2021 derived by integrating Sentinel-1 InSAR and GPS observations
- A two-step InSAR tropospheric correction method used to mitigate both short- and long-wavelength tropospheric effects
- An improved plate spreading model and a revised glacial isostatic adjustment model are presented

Abstract Large-scale ground deformation in Iceland is dominated by extensional plate-boundary deformation, where the Mid-Atlantic Ridge crosses the island, and by uplift due to glacial isostatic adjustment from thinning and retreat of glaciers. While this deformation is mostly steady over multiple years, it is modulated by smaller-scale transient deformation associated with e.g., earthquakes, volcanic unrest, and geothermal exploitation. Here we combine countrywide Sentinel-1 interferometric synthetic aperture radar (InSAR) data (from six tracks) from 2015 to 2021 with continuous GPS observations to produce time-series of displacements across Iceland. The InSAR results were improved in a two-step tropospheric mitigation procedure, using (1) global atmospheric models to reduce long-wavelength and topography-correlated tropospheric signals, and (2) modeling of the stochastic properties of the residual troposphere. Our results significantly improve upon earlier country-wide InSAR results, which were based on InSAR stacking, as we use more data, better data weighting, and advanced InSAR corrections to produce time-series of ground displacements instead of just velocities. We fuse the three ascending and three descending track results to estimate maps of near-East and vertical velocities, which clearly show the large-scale extension and GIA deformation. Using a revised plate-spreading and glacial isostatic adjustment models, based on these new ground velocity maps, we remove the large-scale and steady deformation from the InSAR time-series and analyze the remaining transient deformations. Our results demonstrate the importance of (1) mitigating InSAR tropospheric signals over Iceland and of (2) solving for time-series of deformation, not just velocities, as multiple transient deformation processes are present.

Plain Language Summary Iceland is continuously deforming due to multiple processes across the country, including both large-scale steady activities (e.g., plate spreading and glacial isostatic adjustment (GIA) from thinning and retreat of glaciers) and small-scale transient processes (e.g., earthquakes, landslides, volcanic and geothermal processes). In this paper, we use seven years (2015 to 2021) of Sentinel-1 interferometric aperture radar (InSAR) data to map time-series of high-resolution ground displacements over Iceland to study both the long- and short-term geodynamic activities. To improve the precision of InSAR-derived displacements, we propose a two-step-based troposphere correction approach to mitigate the tropospheric delays that pollute the InSAR displacements. Using the improved displacements, we estimate the countrywide movements at horizontal (i.e., near-East) and vertical directions. Based on the horizontal and vertical displacement fields, we revise the plate-spreading and the GIA models, and we study the transient deformations caused by earthquakes, volcanoes, and landslides. Our study demonstrate the capability of InSAR in study nationwide spatio-temporal geodynamic activities.

1. Introduction

Located on the plate boundary between the North American and Eurasian plates, Iceland is the only part of the Mid-Atlantic Ridge that rises above sea level. The present active plate boundary crossing the island consists of a series of seismic and volcanic rift zones, in a configuration influenced by interactions between the mid-oceanic ridge and excessive mantle upwelling (e.g., Sigmundsson et al. 2020). As a result, Iceland is continuously deforming associated with various geodynamic processes, including plate spreading (e.g., Sigmundsson 2006, Einarsson 2008), seismic activity (e.g., Jónsson et al. 2003, Hreinsdóttir et al. 2009), and volcanic unrest (e.g., Thordarson and Larsen 2007, Sigmundsson et al. 2015). Due to thinning and retreat of the Icelandic ice caps since the end of the Little Ice Age, glacial isostatic adjustment (GIA) is an additional major process that causes crustal deformation over most of Iceland (e.g., Árnadóttir et al. 2009, Auriac et al. 2013, Drouin and Sigmundsson 2019). Given the range of spatio-temporal scales of the deformation in Iceland, it is thus critical to map the deformation in as high resolution as possible, in both space and time, to enable separation of the various deformation signals due to the different underlying processes.

Interferometric synthetic aperture radar (InSAR) has been extensively used to study different deformation processes in Iceland. For example, plate boundary deformation in Southwest Iceland (Vadon and Sigmundsson 1997), North Iceland (Metzger and Jónsson 2014), and in the northern volcanic zone (Pedersen, Sigmundsson and Masterlark 2009) have been explored. Different SAR datasets have been used to capture smaller-scale deformation, e.g., due to earthquakes in South Iceland (e.g., Sudhaus and Jónsson 2009, Decriem et al. 2010, Jónsson et al. 2020), at volcanoes (e.g., Pedersen 2004, Pedersen and Sigmundsson 2005, Ofeigsson et al. 2011, Li et al. 2021), and in geothermal areas (e.g., Keiding et al. 2010, Drouin et al. 2017b). Furthermore, GIA deformation around the largest ice cap in Iceland, Vatnajökull, has also been captured and studied with InSAR (Auriac et al. 2013, Auriac et al. 2014). These studies have demonstrated that the conditions in Iceland for studying small and large spatial-scale deformation with InSAR are favorable as the revisit times are short, due large overlap between parallel tracks at this high latitude and because interferometric coherence is generally high due to limited vegetation, although snow prevents observations during the winter months.

Drouin and Sigmundsson (2019), for the first time, mapped in high-resolution (~100 m) countrywide deformation velocities (i.e., rates) of Iceland by using four years (2015-2018) of Sentinel-1 data acquired in summer. By using stacking of InSAR images, they found that both large-scale signals (plate spreading, GIA) and small-scale signals (e.g., volcanic, geothermal) could be well retrieved with satisfactory precision. While they demonstrated the capability of using InSAR stacking to estimate line-of-sight (LOS) deformation rates, stacking only provides the average deformation rates during a study period, meaning that deformation transients and other nonlinear processes are not correctly retrieved. In addition, possible interferogram unwrapping errors can cause large biases in InSAR stacking rates, which are not easily detected. Furthermore, temporal correlations between the interferograms are not considered, which affects the accuracy of the estimated rates. And finally, tropospheric delays can cause up to ~ 30 cm of non-tectonic signals in interferograms (Cao et al. 2017), affecting estimated deformation rates (Cao, Jónsson and Li 2021a), particularly over large areas with significant topography, that are not optimally reduced by stacking multiple interferograms.

Here we map countrywide displacements in Iceland using Sentinel-1 InSAR data and improve on the earlier study by Drouin and Sigmundsson (2019) in the following ways: 1) a

longer time period of Sentinel-1 data from 2015 to 2021 is used, 2) time-series evolution of the countrywide displacements is estimated, 3) a two-step tropospheric correction is used to reduce long-wavelength and topography-correlated tropospheric signals, and the stochastic properties of the residual troposphere are modeled for better deformation rate estimation, 4) potential accelerations in time-series of vertical displacements are analyzed and discussed, and 5) the reliability of the InSAR results (displacement time-series and rates) are evaluated based on phase closures of the interferograms.

2. Data processing

2.1 Interferograms and time-series InSAR processing

For the data processing, we selected Sentinel-1 data acquired over seven years from 2015 to 2021 and used images between May and November to avoid winter snow. To achieve a full country-wide coverage, data from three descending (tracks 155, 9, and 111) and three ascending (tracks 16, 118, and 147) orbital tracks are needed (Figs. 1 and S1). This selection criteria yielded over 170 SAR images for each of the 6 tracks and 1061 SAR images in total. As each SAR image is generated from 3 standard Sentinel-1 data (or frames, from south to north), the total number Sentinel-1 data products we downloaded is over 3000. In addition to the Sentinel-1 data, time-series from more than 150 continuous GNSS sites (Fig. 1), were used to estimate reference shifts between tracks and to correct for possible orbital errors in the InSAR time-series analysis (Cao et al. 2021b).

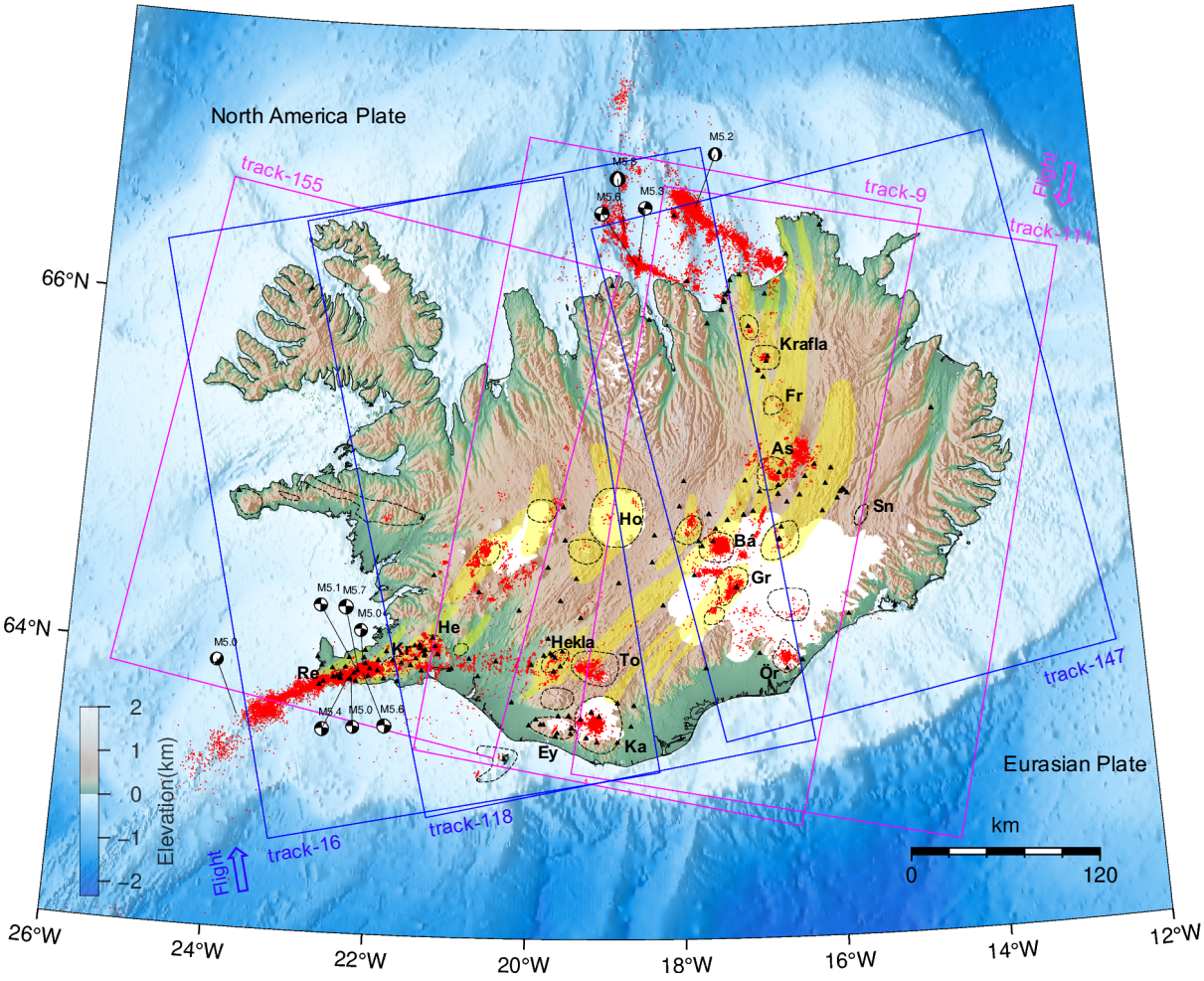

Figure 1. Map of Iceland showing ice caps (white areas), earthquake locations (M>1) between June 2015 and October 2021 (red dots), volcanic systems (yellow areas and dashed black lines), and locations of continuous GNSS stations (black triangles). The three blue and three magenta rectangles show the coverage of the ascending and descending Sentinel-1 tracks used in this study. Black beach balls indicate locations and focal mechanisms of the eight M ≥ 5 earthquakes that occurred during the study period. (Re=Reykjanes, Kr=Krísuvík, He=Hengill, Ey=Eyjafjallajökull, Ka=Katla, To=Torfajökull, Ho=Hofsjökull, Ör=Öræfajökull, Bá = Bárðarbunga, Gr = Grímsvötn, Sn = Snæfell, As=Askja, Fr=Fremrinámar.

We processed the interferograms using the open source toolbox PyINT (PYthon-based INterferometry Toolbox) (Cao et al. 2021a) that we developed to automate processing with the GAMMA software (Wegnüller et al. 2016). Although each track includes three standard Sentinel-1 images, about a third of the bursts are located in water or ocean areas, only land-based bursts were extracted and used to improve the processing efficiency. We used the POD Precise Orbit Ephemerides (AUX_POEORB) data to limit orbital ramps in the InSAR data and the ESA Copernicus 30 m DEM to remove the topographic phases. We applied an improved version of the Goldstein filter (Li et al. 2008) and multilooking (30 and 8 looks for the range and azimuth directions) to reduce decorrelation noise, yielding spatial pixel spacing of about

100 m. Finally, a minimum cost flow algorithm was used to unwrap the interferograms (Werner et al. 2002). For the interferogram network, we employed a combined small-baseline and bridging approach to ensure all the interferometric pairs were included in one network. We achieved this by first selecting all the small-baseline pairs with spatial and temporal baselines less than 120 m and 50 days, respectively, and then bridging yearly sub-networks by connecting July and August pairs with spatio-temporal baselines smaller than 120 m and 14 months. In total, we generated 8699 interferograms based on the 1061 SAR images (Fig. 2).

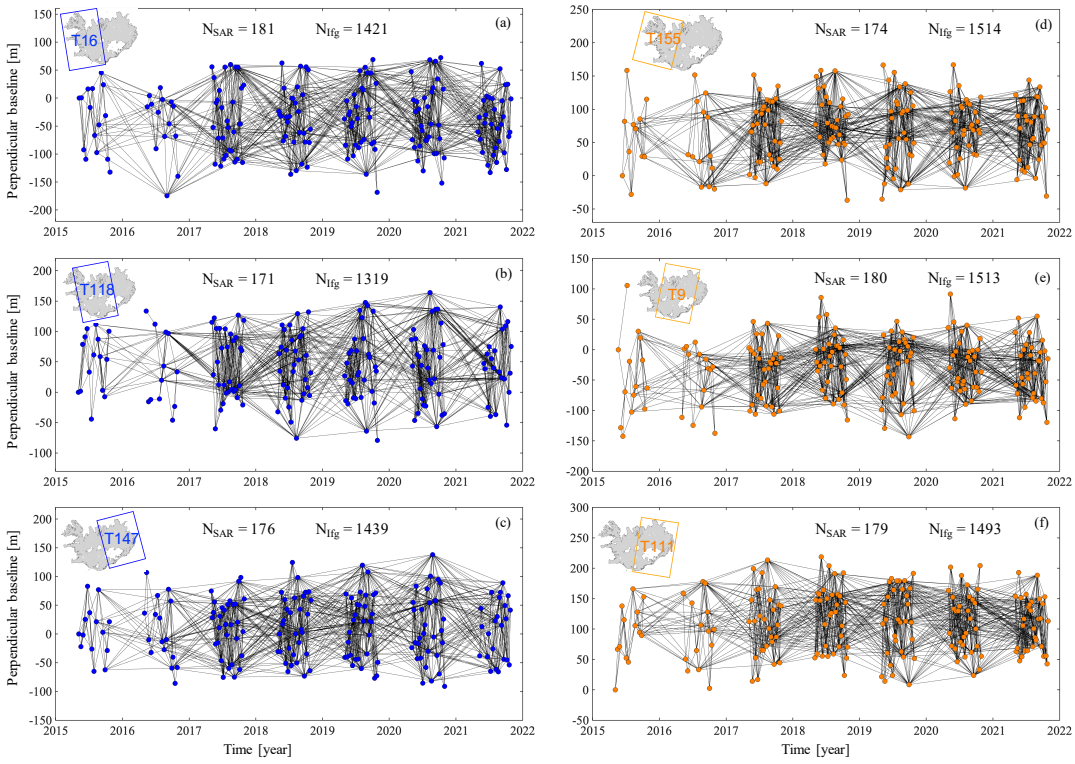

Figure 2. Spatio-temporal baseline plots of the interferograms for the three ascending (left) and three descending (right) tracks. The top-left subplot in each panel shows the coverage of the SAR data, with N_{SAR} and N_{ifg} indicating the number of SAR images and generated interferograms for each track.

Before estimating the InSAR time-series, we tied the unwrapped interferograms of each track to the same reference point near the middle of the SAR image coverage, where the averaged coherence is larger than 0.95. Interferograms with averaged spatial coherence of the ground pixels lower than 0.8 were removed. Considering that snow-free areas in Iceland are generally highly coherent in the interferograms, we did not consider possible effects of decorrelation noise on the time-series inversion, i.e., we used the same weight for all the

interferograms. As all the used interferograms of each track were included in one network, we solved the time-series using standard least-squares.

To improve the estimated InSAR time-series, we propose a two-step tropospheric signal reduction: first, we estimate tropospheric delays for time-series of SAR acquisitions with the open source toolbox ICAMS (https://github.com/ymcmrs/ICAMS) that uses global atmospheric model outputs (Cao et al. 2021a), and second, we model the spatio-temporal variance components of the residual tropospheric delays (after correction) using the network based variance-covariance estimation (NVCE) algorithm (Cao et al. 2017), for better estimating LOS deformation rates.

Tropospheric delays are significant in the raw InSAR time-series solutions (Fig. S1-S6), despite they are generally weaker at this high latitude region than at mid- and low-latitudes. The ICAMS correction considerably improves the time-series solution (Fig. S7-S12), albeit strong residual tropospheric signals remain in several of the SAR images. Modeling of the stochastic properties of the residual tropospheric delays shows the tropospheric effects strongly vary for different SAR acquisitions (Fig. S13-S17, Fig. 3), which indicates the importance of considering tropospheric variances when estimating parameters based on the time-series solution (e.g., velocity, seasonal amplitude). The tropospheric variances (after ICAMS correction) of e.g., track-9 (Fig. 3) grow with the distance from the reference pixel but are lower than 2 cm^2 for most of the SAR images. For some images the variances are larger, i.e., over 6 cm^2, and for the image of 19 July 2021 even up to 10 cm^2. Note that here the tropospheric variance is associated with the absolute tropospheric delays in each SAR acquisition (Cao et al. 2017), and not the differential tropospheric delays observed in the interferograms.

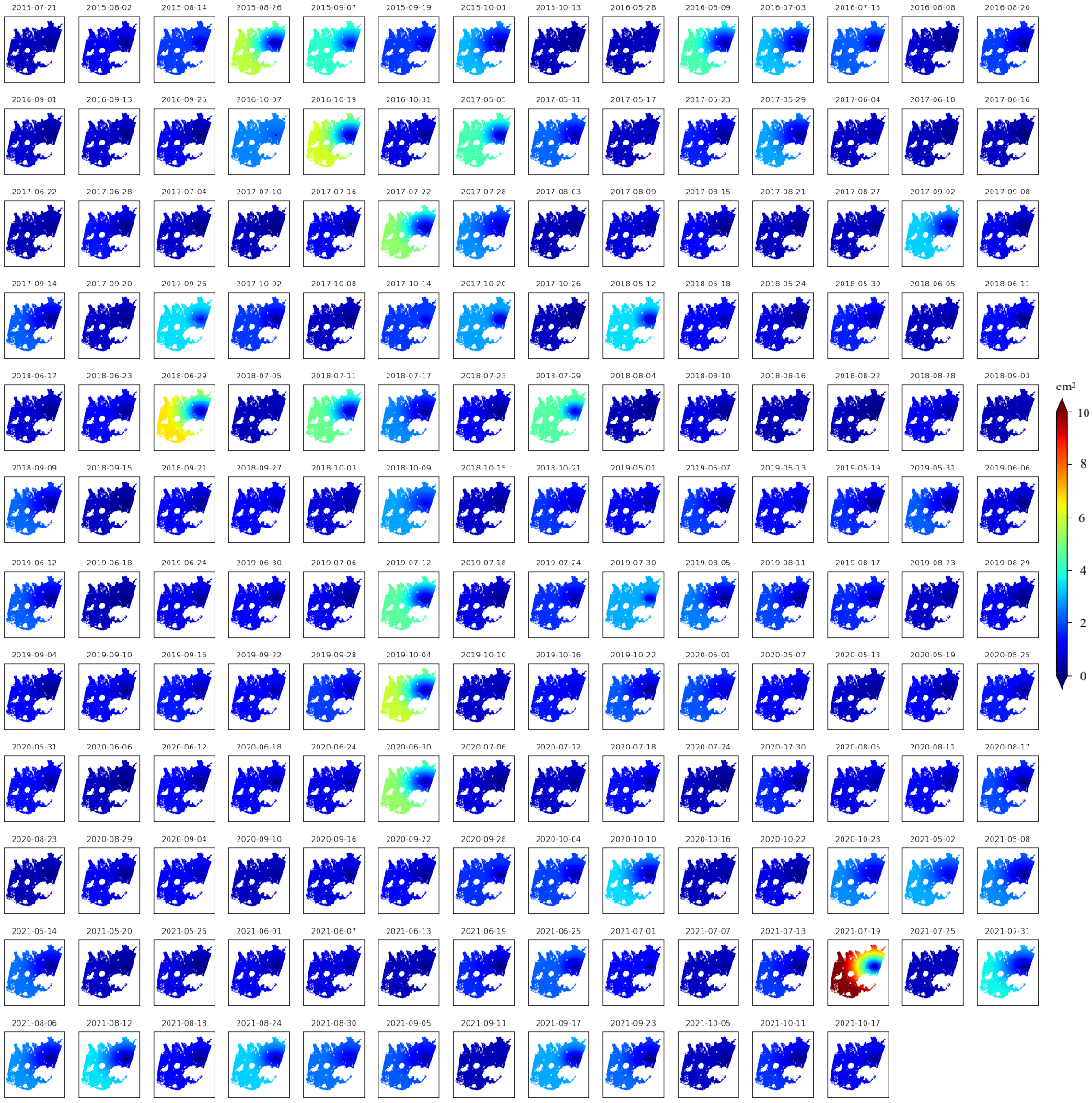

Figure 3. Spatio-temporal tropospheric variances (after ICAMS correction) in SAR acquisitions of track-9 (example).

2.2 Integration of InSAR and GPS measurements

Time-series of the GNSS site positions were first estimated in the ITRF2020 reference frame and we then referenced them to the Eurasian plate. For each SAR track, we selected and used the GNSS stations that met the following conditions of 1) having observations that cover the same period as the SAR time-series from June 2015 to October 2021 and 2) being located in an area where the temporal coherence (Lauknes, Zebker and Larsen 2011) of the InSAR estimations is higher than 0.8. We estimated the East, North, and Up velocities of each GNSS station using least-squares estimation of observations between June 2015 and October 2021, and then we calculated the GPS velocity along the InSAR LOS direction site by site (Wright

2004). We model the differences between InSAR- and GPS-derived LOS velocities to adjust the InSAR results for reference shift and possible large-scale long-wavelength signals (due to possible orbital errors and residual tropospheric delays) by using a first-order surface function (Cao et al. 2021b).

The InSAR LOS velocities (June 2015 to October 2021) for the six different tracks are presented in Figure 4, with areas with temporal coherence (Fig. S18) lower than 0.75 masked. The standard deviation (STD) of InSAR LOS velocity was estimated for each track by taking the GPS-derived LOS velocity as an error-free value. All of the STDs (shown by σ in Fig. 4) of the six tracks are smaller than 2 mm/yr. The average STD values of the ascending and descending results are ~1.4 mm/yr and ~1.6 mm/yr, respectively, indicating that the results from both look directions are highly consistent with the GPS measurements. Note that due to the large differences in the incidence angles of Sentinel-1 between near- and far-range of the satellite swath coverage (i.e., from ~30 degrees to ~45 degrees), the LOS velocities of adjacent tracks are not the same.

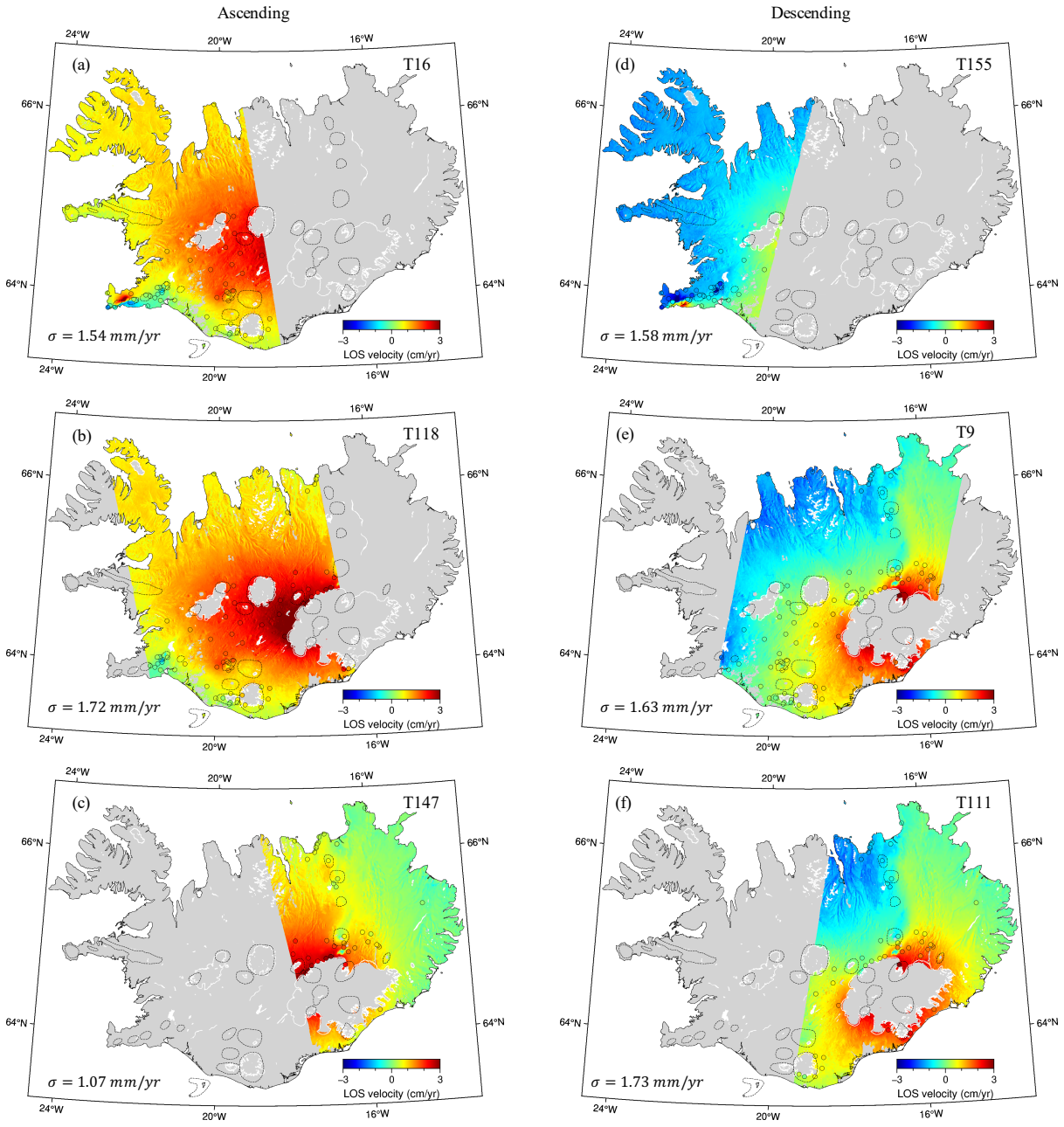

Figure 4. InSAR line-of-sight (LOS) velocities for the three ascending tracks (left) and three descending tracks (right). Colored circles indicate GNSS-derived LOS velocities with the standard deviation (σ) of InSAR LOS velocities reported for each track. The white lines are edges of the ice caps and dashed black lines are edges of central volcanoes.

2.3 Estimation of countrywide near-East and near-Up deformation

As the Sentinel-1 InSAR observations are relatively insensitive to the horizontal displacements in the North direction, we estimate the near-East and near-Up movements by combining the ascending and descending velocities and ignoring the North-movements (Wright 2004). To do so, we first resample the six tracks of the InSAR results into the same

countrywide coordinate system and mask those measurements where the temporal coherence values are lower than 0.7. We then estimate the near-East and near-Up velocities, pixel by pixel, using least-squares estimation of all the available measurements (two to four) at each location. For this estimation, we use a minimum of two measurements (one ascending and one descending), but for some areas up to four measurements, where two ascending and two descending tracks overlap (see SAR image coverage in Fig. 1).

The countrywide results of near-Up and near-East velocities (Fig. 5a-b) show that GIA signals around the Vatnajökull ice cap and in central Iceland dominate the near-Up velocity map and reach up to 30 mm/year, whereas the near-East velocities clearly exhibit the extension at the plate boundary. To evaluate the precision of these results, we compare GPS- (colored circles in Fig. 5a-b) and InSAR-derived velocities in the Up and East directions. The standard deviation of the differences between InSAR and GPS velocities in the two directions are 1.8 mm/year and 1.9 mm/year (see histogram in Fig. 5a-b), respectively, compared with that of 3.3 mm/year and 2.4 mm/year by Drouin and Sigmundsson (2019). This indicates that the longer time-series and the tropospheric corrections yield improved near-Up and near-East velocities.

3. Observed deformation and modeling

3.1 Large-scale and temporally stable deformation

The observed large spatial-scale deformation in Iceland is dominated by GIA and plate spreading (Fig. 5a-b), as stated above. This deformation is also temporally relatively stable, i.e., roughly linear in time. The GIA uplift is due to the present-day thinning of the Icelandic ice caps and ice retreat since 1890 (e.g., Björnsson and Pálsson 2008, Schmidt, Lund and Hieronymus 2012, Drouin et al. 2017, Sigmundsson et al. 2020). The plate spreading signal clearly shows the roughly east-west relative movement and the boundary between the two major lithospheric plates, the North American and Eurasian Plates (e.g., DeMets, Gordon and Argus 2010, Argus et al. 2010).

To model the GIA uplift, here we use the same scaled method as in (Drouin et al. 2017, Drouin and Sigmundsson 2019), which considers a proportional relationship between the geodetic observations and the GIA model by Auriac et al. (2014). This GIA model uses an ice-thinning model and a three-layer Earth model with a thin elastic layer at top (1 km-thick,

Poisson's ratio v = 0.17, Young's modulus E = 14 GPa), another elastic layer in the middle (21-km-thick, v = 0.25, E = 74 GPa), underlain by a viscoelastic medium (v = 0.25, E = 74 GPa, viscosity $\eta = 8.4 \times 10^{18}$ Pa s). By comparing InSAR and predicted GIA velocity profiles in different regions, Drouin and Sigmundsson (2019) showed that scaling the model velocities by 1.3-1.4 best fits the countrywide observations (misfit σ=3.38 mm/year). Previously, Drouin et al. (2017) had found that an even higher scale factor of 1.8 was needed to fit campaign GPS data in the Northern Volcanic Zone (NVZ). Here we systematically analyze the correlation between the countrywide InSAR and GIA-model vertical velocities, instead of evaluating scale factors along different profiles, and fit a linear model using least squares estimation (Fig. S19). We find that scaling of the GIA model displacements by 1.47 (Fig. 5c) provides the best fit to the InSAR velocities (misfit σ=2.7 mm/year), leading to relatively unbiased residuals (Fig. 5e).

To model the plate spreading deformation, we use a backslip model that assumes vertical dislocations from the surface to a hypothetical locking depth and assigs half the plate rate to each side of the plate boundary (e.g., Metzger, Jónsson and Geirsson 2011, Drouin and Sigmundsson 2019). We divide the countrywide measurements into multiple segments along the plate boundary and estimate the model parameters for each segment. The GIA also causes large horizontal movements (e.g., Drouin et al. 2017) that influence the estimation of plate spreading model, if not considered as well. Therefore, we also estimate a scaling factor for predicted horizontal GIA motions (Auriac et al. 2014), yielding a factor of 2.9, and correct the near-East measurements.

We estimate the optimal plate spreading parameters using the GIA-corrected near-East velocity field and the refined plate boundary by Drouin and Sigmundsson (2019) as initial boundary location. We first extracted near-East velocities along multiple country-wide profiles (2 km spacing) crossing the plate boundary segments, profiles with azimuths of N135°E in the South and N104°E for the rest of the segments. Each profile measurement is described by two values, i.e., the distance to the center point (initial plate boundary location) and the near-East velocity. After that, we resampled the profile velocities every 2-km along the profiles using an averaging method to reduce the effects of local deformation and noise. Using these resampled measurements, we estimated the backslip model parameters, i.e., the spreading velocity,

locking depth, and shift of the center point, using a grid-search approach. Collectively, we find that a velocity of 18.0 mm/year provides the best fit to the profile measurements. Note that here the plate velocity means that of the East component, and the full velocity on the spread direction (N100°E - N110°E) should be slightly larger than this value. After determining the best plate velocity, we use a least-squares method with constrained bounds (the locking depth: 1 to 20 km, the shift: -20 to 20 km) to estimate the other two parameters. Using the determined optimal parameters for all of the profiles (see Fig. S20), we refine the plate boundary location (red line in Figure 5d) and produce a model near-East velocity field (Fig. 5d), which includes both the plate spreading and GIA models. The standard deviation of the residuals is 2.3 mm/year (see histogram, in Fig. 5f), compared with that of 3.17 mm/year by Drouin and Sigmundsson (2019).

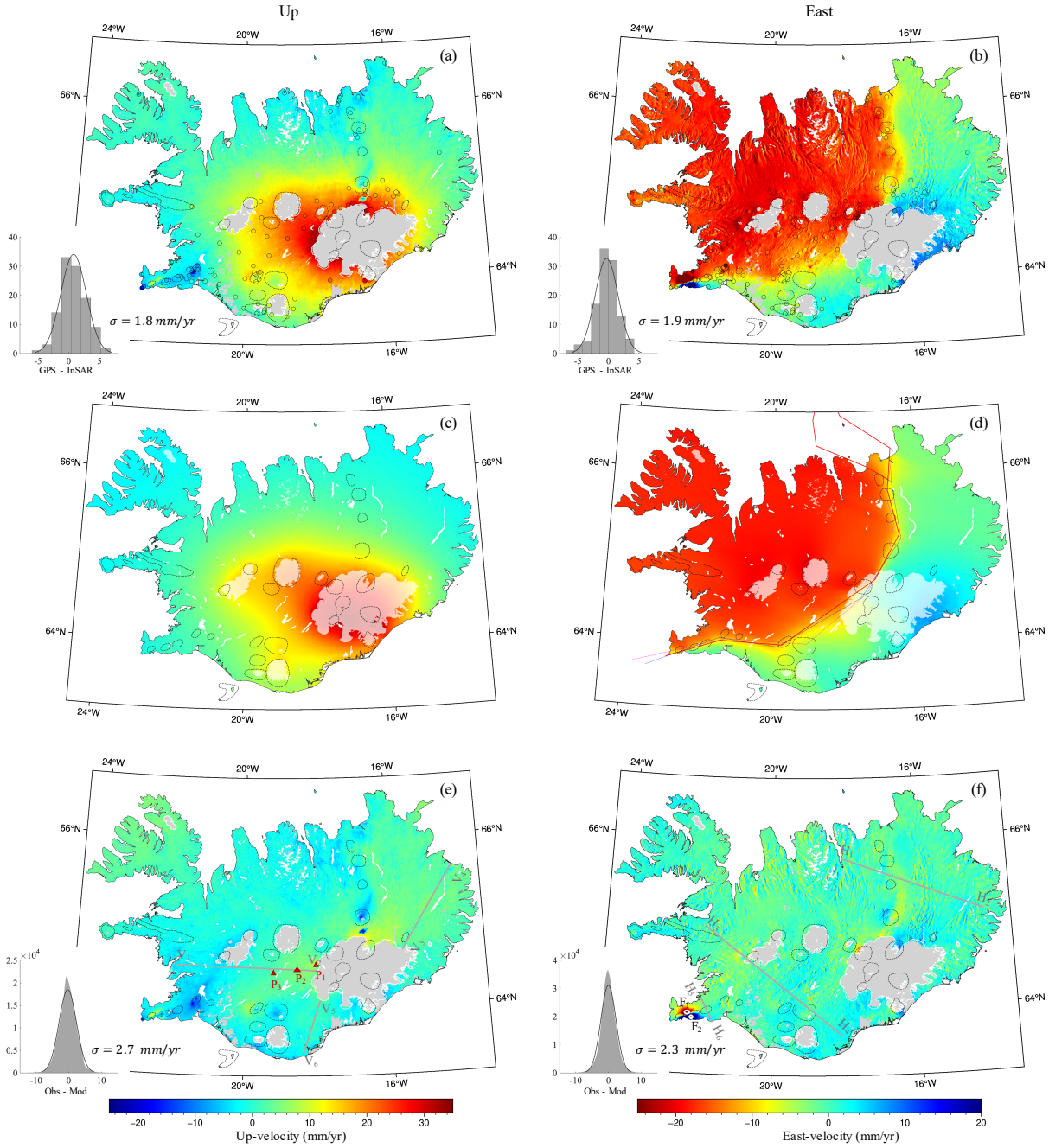

Figure 5. Observed and modeled near-up and near-East velocities. (a) and (b) are observed near-up and near-East velocities, with the histograms indicating the differences between InSAR and GPS. (c) is the modeled vertical GIA velocity and (d) is the reconstructed near-East velocity associated with GIA and plate spreading models. The red lines mark our updated plate boundary location, while thin blue and magenta lines are the boundaries used by Drouin and Sigmundsson (2019) and several earlier studies (Geirsson et al. 2012, Metzger and Jónsson 2014, Drouin et al. 2017), respectively. (e) and (f) are the differences between the observed velocities in (a) and (b) and model predictions in (c) and (d), with the histograms showing the spread of the residuals.

Comparisons between the InSAR derived velocities (near-up and near-East velocities) and model velocities along different profiles across the country (see profile locations in Fig. 5e-f) are presented in Fig. 6. The near up-velocity along the West profile (Fig. 6a) indicates that the vertical GIA-scale is slightly underestimated, whearas the East- and the South-profiles (Fig. 6b-c) show a good agreement between observed and modeled velocities, despite a small bias of 1 to 2 mm/yr along the East profile (Fig. 6b). The near-East velocity profiles all show a fairly good agreement between InSAR-derived and modeled (GIA and plate spreading) velocities, showing significant differences in the widths of the plate boundary deformation zone in the three regions.

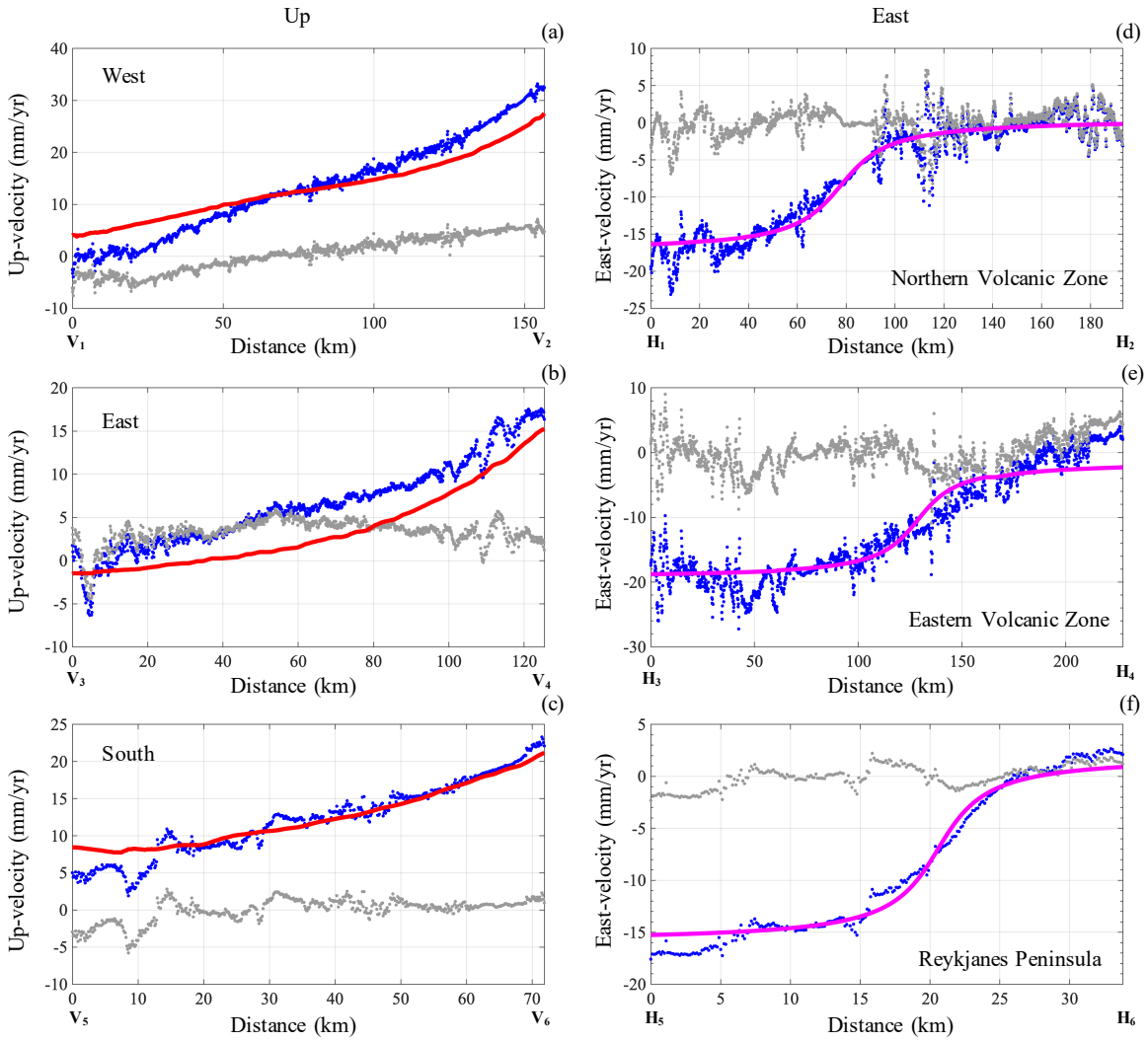

Figure 6. (a)-(c) comparison between near-up InSAR and model velocities along three different profiles (West, East, and South, see Fig. 5e for profile locations). (d)-(f) comparison between near-East InSAR and model velocities along three different profiles (Northern volcanic zone, Eastern volcanic zone, and Reykjanes Peninsula, see Fig. 5f for profile locations). Blue, red/magenta, and gray dots are InSAR data, model values, and residuals, respectively.

3.2 Small-scale and temporally variable deformation

Many small spatial scale deformation signals are visible in the residual velocity maps (Fig. 5e and 5f), which are mostly caused by pressure changes in geothermal areas or volcanic activity, particularly by the 2021 Fagradalsfjall eruption on Reykjanes Peninsula. In addition, widespread slope movements can be seen on most west- and east-facing slopes (Fig. 5f), peaking at locations that have notable landslides. While detailed geophysical analysis of these local signals is beyond the scope of this study, we here describe the temporal evolution of small-scale deformation in several areas of interest that include volcano, geothermal, and landslide deformation.

Time-series of near-up and near-East displacements at Fagradalsfjall volcano show strong uplift in 2020 of around 9 cm (compared to 2019) and large westward movement in 2021 of ~15 cm to the northwest of the volcano (Fig. 7a, locations in Fig. 5f) and strong eastward movement (~ 25 cm) to the south (Fig. 7b) in 2021, due to 2021 magma intrusion and earthquake activity in Reykjanes. At the Reykjanes geothermal area (Fig. 7c), steady subsidence of ~2 cm/year increased to ~5 cm/year in 2020 and then slowed to ~1 cm/year from July 2020, changes related to the volcanic and earthquake activity on the peninsula. Subsidence at the Hengill geothermal area (Fig. 7d) is more stable with a steady subsidence of ~1.6 cm/year during the observation period. Torfajökull volcano shows a clear change from subsidence during 2015-19 of ~1.5 cm/year (Fig. 7e) to sharp uplift of 7 cm/year in 2019, which then changed to subsidence again by the end of 2019. Displacements observed at Öræfajökull volcano (Fig. 7f) are relatively weak, albeit with moderate uplift during 2017-20 of ~1.7 cm/year. Askja volcano, located just north of Vatnajökull ice cap, was steadily subsiding 2015-21 by ~1.8 cm/year, which turned to rapid uplift from the middle of 2021 of ~1 cm/day, likely related to magma accumulation under Askja (Nobile et al., 2022). In addition to volcanic and geothermal deformation, widespread slope creep is visible in the near-East velocity residual map, creep that is at fairly stable velocity in most places. Time-series displacement of one

example landslide, located at North Iceland, shows however that this landslide started to move in 2017 (~1.8 cm/year) with notable seasonal variations in movement.

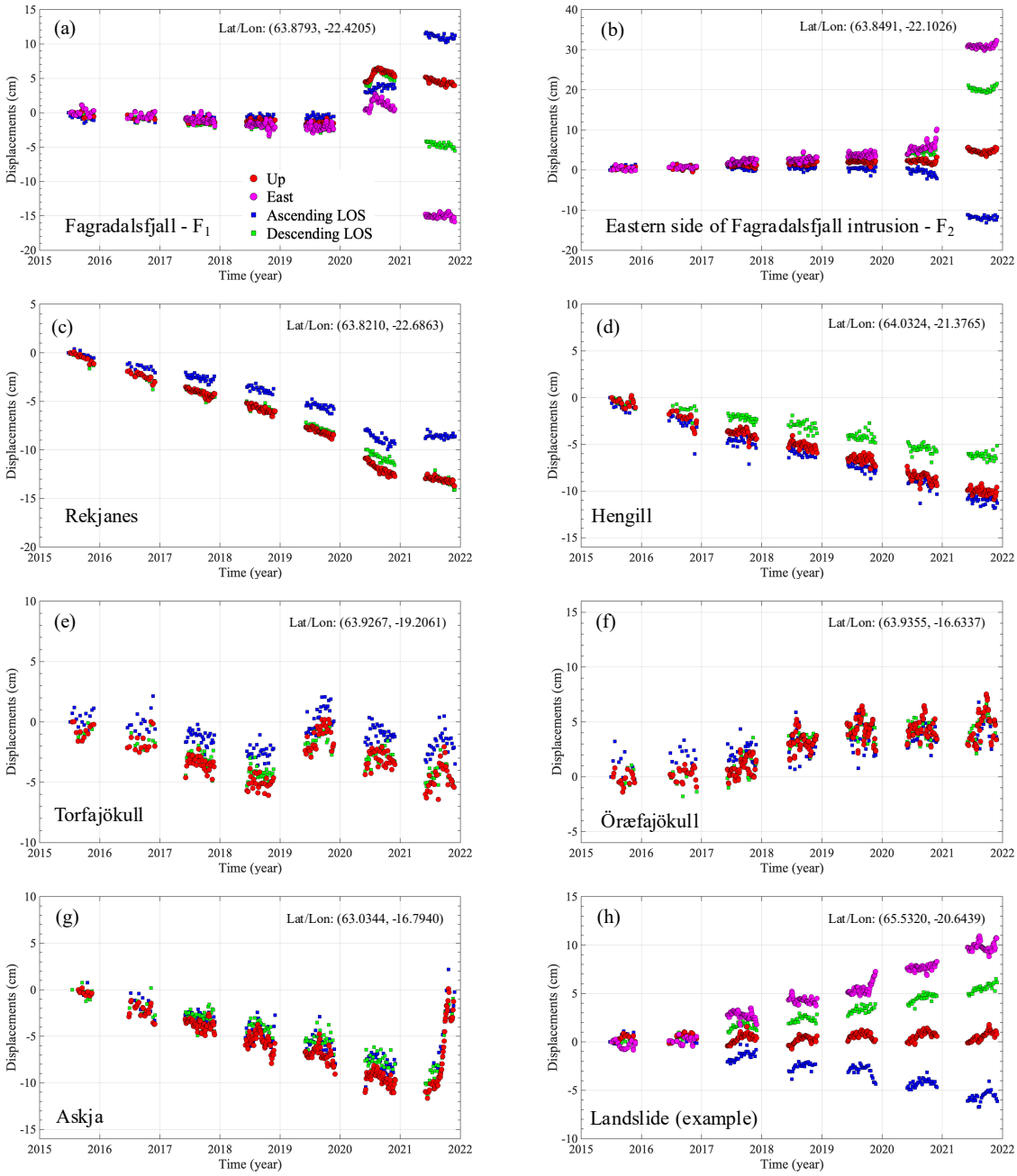

Figure 7. Time-series displacements of small spatial scale deformation processes: (a)-(b) northwest and southeast of the Fagradalsfjall volcano, (c) and (d) Reykjanes and Hengill geothermal areas. (e), (f), and (g) Torfajökull, Öræfajökull, and Askja volcanoes. (h) example landslide in North Iceland. Each location is indicated (top right) and red, magenta, blue, and green circles represent InSAR-derived vertical, East, ascending-, and descending-LOS displacements, respectively.

4. Discussion

4.1 Importance of correcting and modeling troposphere for Iceland InSAR applications

Large spatial-scale deformation (e.g., GIA or plate spreading) in Iceland is mostly linear in time, albeit modulated by seasonal signals due to winter snow loading. Velocity uncertainties (i.e., standard deviation) estimated based on residuals of the time-series displacements from a linear model are thus dominated by temporal variations of tropospheric delays, although some of the uncertainty could be caused by transient displacements (e.g., local displacements as presented in Fig. 7) and other observation errors. Therefore, the velocity uncertainties can be used to evaluate the tropospheric effects on the time-series.

We compare velocity uncertainties of one example track (track 9) estimated for velocities from three different times-series solutions (raw, ICAMS-corrected, and ICAMS-corrected with NVCE stochastic modeling) based on both four years of data (2015-2018) and seven years of data (2015-2021). The velocity uncertainty improves significantly (>50% improvement) by extending the data set from four years (as in Drouin and Sigmundsson (2019) to seven years (Fig. 8a-b); the maximum uncertainty reduces from ~ 5 mm/year to ~ 2 mm/year, when using the raw uncorrected time-series to estimate the velocity. Additional improvement is achieved (also ~50%) by using the ICAMS atmospheric corrections, with the uncertainty reducing further to ~2.5 mm/year (from ~5 mm/year) and to ~1 mm/year (from ~2 mm/year), respectively, for the four- and seven-year datasets (Fig. 8c-d). After considering NVCE stochastic modeling of the residual tropospheric delays, further improvement of the velocity uncertainty can be seen (Fig. 8e-f), although the improvement is relatively small compared with that achieved by the steps above.

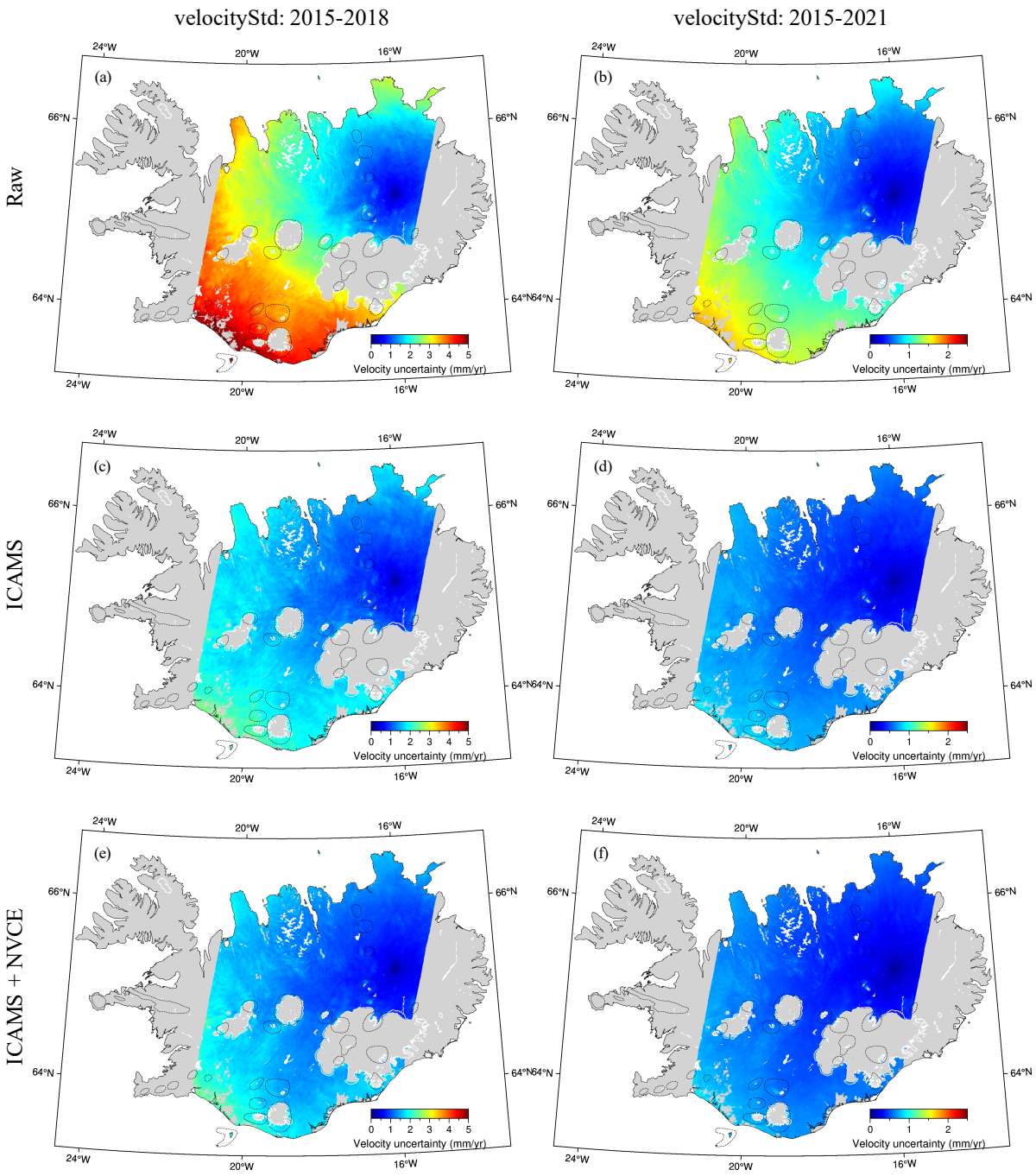

Figure 8. Velocity uncertainties (i.e., standard deviation, STD) of example track 9 estimated from different time-series solutions: (a) and (b): from raw time-series based on datasets spanning 2015-2018 and 2015-2021, respectively. (c) and (d): from ICAMS-corrected time-series, and (e) and (f) from two-step tropospheric correction (ICAMS+NVCE) time-series.

Another way to assess the velocity improvement of the tropospheric corrections is to compare the results with velocities at continuous GPS stations, assuming the GPS-derived LOS velocities are relatively free of errors (Fig. 9). On average, we find that with the ICAMS correction the STD of the difference between the GPS and InSAR velocities is reduced from

1.72 mm/year to 1.62 mm/year. The STD of the velocity differences reduces further to 1.54 mm/year if the NVCE stochastic modeling is included in the InSAR time-series solution. Similar improvements can be found from the statistical results of mean absolute error (MAE). While this demonstrates the success of the tropospheric corrections, assuming the GPS-LOS velocities are error free is somewhat misleading, as they in fact contain significant uncertainties themselves and then the GPS stations are also not uniformly distributed in the area of interest. Therefore, the estimation of the STD (or MAE) of the velocity differences could be biased to some degree.

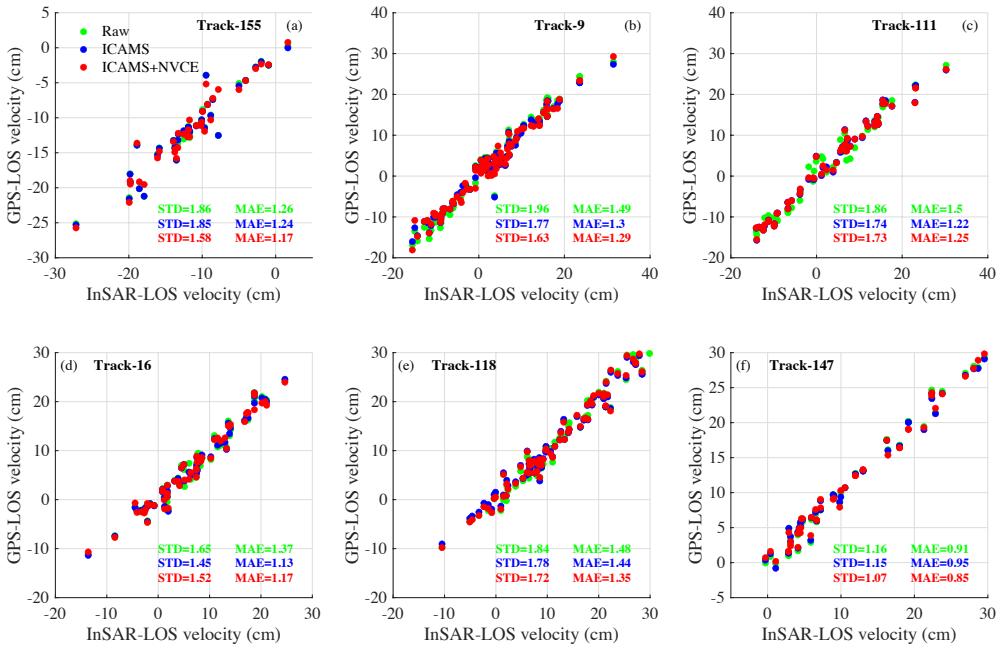

Figure 9. Comparison of GPS-derived LOS velocities and InSAR LOS-velocities (from all the six tracks) derived from raw uncorrected time series (green), ICAMS corrected time series (blue), and time-series after ICAMS correction with NVCE (red) stochastic modeling (ICAMS+NVCE), with "STD" values indicating the standard deviations of the difference.

4.2 Possible acceleration of uplift in Iceland

Acceleration of uplift in central Iceland was observed at multiple GPS stations in data from before 2014 and linked to increasing mass loss rate of the Icelandic ice caps (Compton, Bennett and Hreinsdóttir 2015). The InSAR time-series of vertical displacements appear to show continuation of this acceleration. We picked time series from three locations (P_1, P_2, and P_3 in Fig. 5e), at different distances from the uplift maximum and thus with different vertical

velocities, and fit to them a second-order polynomial that includes annual variations, using standard least-squares (Fig. 10). All three time-series indicate considerable accelerations of 1.66, 1.37, and 1.07 mm/year^2 for locations P_1, P_2, and P_3, respectively. Our results are consistent with Compton et al. (2015), who also reported 1 to 2 mm/year^2 uplift accelerations in central Iceland. This indicates that the uplift rate continues to increase with similar uplift accelerations estimated from GPS for 2000-2015 and from InSAR data from 2015 to 2021. To verify the continued uplift acceleration, we used an *F* test (Bevington and Robinson 2003) to assess the significance of including an acceleration term in the polynomial fit, similar to that used by Compton et al. (2015). We found the F_χ values at the three points reach 56.1, 85.7, and 78.2, respectively, and the *p*-values are all less than 0.01, indicating that all three time-series exhibit significant accelerations at the 99% confidence level. The results demonstrate the potential of using InSAR time-series to monitor gradual changes of vertical displacement rates in response to large-scale mass changes .

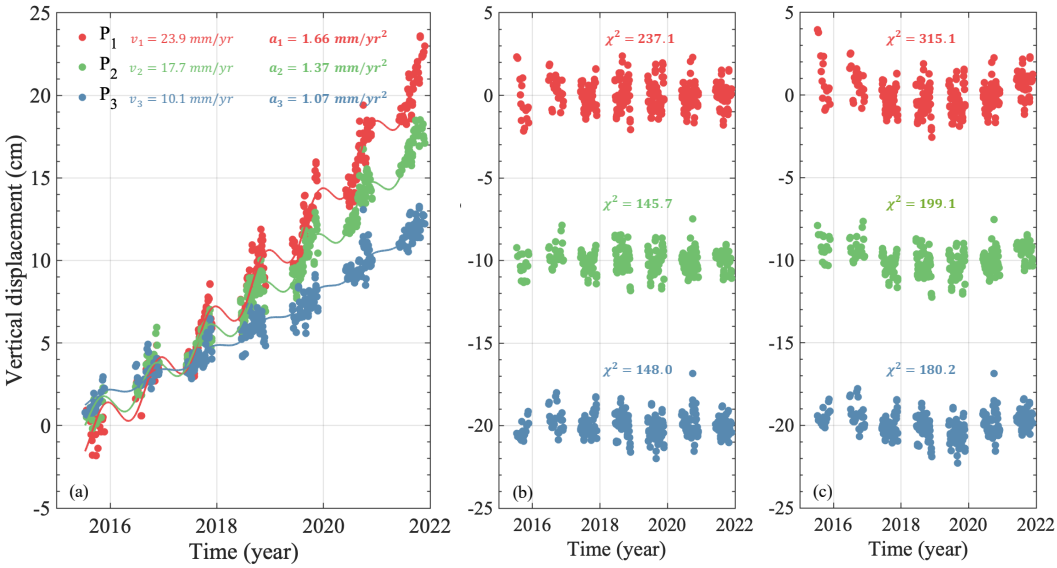

Figure 10. Evaluation of possible uplift accelerations at three locations P_1, P_2, and P_3 (see Fig. 5e). (a) Uplift time-series and model fit using a second-order polynomial function with annual variations at the three locations. (b) Residuals from the model (second-order polynomial + annual) that considers acceleration, and (c) residuals from the model (linear + annual) that does not consider acceleration. Residuals for P_2 and P_3 are shown offset to -10 cm and -20 cm, respectively, for display clarity.

4.3 Challenges of detecting seasonal deformation in Iceland with InSAR

GPS time-series in Iceland exhibit strong seasonal signals, particularly in the vertical component, with the seasonal amplitudes ranging from ~4 mm near the coast to up to 27 mm in the central part of the country. The seasonal signals are mostly due to seasonal snow loading variations (Drouin et al. 2016). Unlike GPS, InSAR only maps relative displacements, meaning observed displacements are with respect to a chosen reference point. Meanwhile, the seasonal deformation is also spatially correlated, although peak snow loading occurs later in the winter at higher elevations (e.g., Drouin et al. 2016), which means we need a reference point as far as possible, if we want to quantify seasonal deformation accurately in the InSAR observations. However, as the atmospheric delays are also spatially correlated, a distant reference point leads to stronger the tropospheric effects on the time-series. To add to the challenge, only Summer images are usable for large parts of Iceland due to Winter snow coverage, making quantification of seasonal signals in the InSAR time-series somewhat unreliable. Therefore, it remains challenging to determine the spatio-temporal variations of seasonal signal amplitudes in InSAR time-series.

5. Conclusion

From 7 years of Sentinel-1 data of 6 different tracks, we derived time-series of countrywide surface displacements over Iceland that exhibit both large-scale temporally stable processes (GIA, plate motions) and small-scale temporally variable activity (e.g., volcanic unrest and earthquakes). We significantly improved, by more than 50%, the derived time-series and estimated velocities with a two-step tropospheric correction approach, demonstrating the usefulness of tropospheric corrections for InSAR applications in Iceland. The standard deviations between the InSAR-LOS and GPS-LOS velocities, from the 6 tracks, are all better than 2 mm/year, and the estimated countrywide near-Up and near-East velocity maps have standard deviations of 1.8 and 1.9 mm/year, respectively. We explain most of the observed velocity field with a combined plate spreading and GIA-model, with a model error of 2.3 mm/year. Residual displacements are mainly due to local deformation associated with active

volcanoes, geothermal exploitation, and landslide movements. We also report acceleration of uplift that reaches ~2 mm/year^2 in central Iceland, showing that the increase in uplift rate seen for 2000-2015 from GPS has continued. Taken together, our study highlights the capability of InSAR for countrywide monitoring of a range of geodynamic activity both in space and time.

Acknowledgements

This research was supported by King Abdullah University of Science and Technology (KAUST), under award number BAS/1/1353-01-01, and public research funding from the Government of New Zealand. The Sentinel-1 images are from the European Space Agency (ESA) and downloaded from the Alaska Sat- ellite Facility (ASF) (https://asf.alaska.edu/data-sets/sar-data-sets/sentinel-1/), and the EAR5 data used by ICAMS are provided by ECMWF (https://www.ecmwf.int/en/forecasts/datasets/reanalysis-datasets/era5). The earthquake data (location and magnitude) is provided by the Icelandic Meteorological Office (IMO) (https://hraun.vedur.is/). Installation and operation of the GPS sites used in this study were led by IMO, University of Iceland, Penn State, ETH, Landmælingar Íslands, Landsvirkjun, Université de Savoie, Bayerische Akademie der Wissenschaften, and KAUST. REYK and HOFN are International GNSS Service stations. UNAVCO and the IMO provided the technical support.

References

Argus, D. F., R. G. Gordon, M. B. Heflin, C. Ma, R. J. Eanes, P. Willis, W. R. Peltier & S. E. Owen (2010) The angular velocities of the plates and the velocity of Earth's centre from space geodesy. *Geophysical Journal International,* 180**,** 913-960.

Árnadóttir, T., B. Lund, W. Jiang, H. Geirsson, H. Björnsson, P. Einarsson & T. Sigurdsson (2009) Glacial rebound and plate spreading: results from the first countrywide GPS observations in Iceland. *Geophysical Journal International,* 177**,** 691-716.

Auriac, A., F. Sigmundsson, A. Hooper, K. H. Spaans, H. Björnsson, F. Pálsson, V. Pinel & K. L. Feigl (2014) InSAR observations and models of crustal deformation due to a glacial surge in Iceland. *Geophysical Journal International,* 198**,** 1329-1341.

Auriac, A., K. H. Spaans, F. Sigmundsson, A. Hooper, P. Schmidt & B. Lund (2013) Iceland rising: Solid Earth response to ice retreat inferred from satellite radar interferometry and visocelastic modeling. *Journal of Geophysical Research: Solid Earth,* 118**,** 1331-1344.

Bevington, P. R. & D. K. Robinson. 2003. *Data Reduction and Error Analysis for the Physical Sciences, McGraw-Hill, .*

Björnsson, H. & F. Pálsson (2008) Icelandic glaciers. *Jökull,* 58**,** 365-386.

Cao, Y., S. n. Jónsson & Z. Li (2021a) Advanced InSAR Tropospheric Corrections From Global Atmospheric Models that Incorporate Spatial Stochastic Properties of the Troposphere. *Journal of Geophysical Research: Solid Earth,* 126.

Cao, Y., Z. Li, M. Duan & J. Wei (2021b) High‐Resolution Water Vapor Maps Obtained by Merging Interferometric Synthetic Aperture Radar and GPS Measurements. *Journal of Geophysical Research: Atmospheres,* 126.

Cao, Y., Z. Li, J. Wei, J. Hu, M. Duan & G. Feng (2017) Stochastic modeling for time series InSAR: with emphasis on atmospheric effects. *Journal of Geodesy,* 92**,** 185-204.

Compton, K., R. A. Bennett & S. Hreinsdóttir (2015) Climate-driven vertical acceleration of Icelandic crust measured by continuous GPS geodesy. *Geophysical Research Letters,* 42**,** 743-750.

Decriem, J., T. Árnadóttir, A. Hooper, H. Geirsson, F. Sigmundsson, M. Keiding, B. G. Ófeigsson, S. Hreinsdóttir, P. Einarsson, P. LaFemina & R. A. Bennett (2010) The 2008 May 29 earthquake doublet in SW Iceland. *Geophysical Journal International*.

DeMets, C., R. G. Gordon & D. F. Argus (2010) Geologically current plate motions. *Geophysical Journal International,* 181**,** 1-80.

Drouin, V., K. Heki, F. Sigmundsson, S. Hreinsdóttir & B. G. Ófeigsson (2016) Constraints on seasonal load variations and regional rigidity from continuous GPS measurements in Iceland, 1997–2014. *Geophysical Journal International,* 205**,** 1843-1858.

Drouin, V. & F. Sigmundsson (2019) Countrywide Observations of Plate Spreading and Glacial Isostatic Adjustment in Iceland Inferred by Sentinel‐1 Radar Interferometry, 2015–2018. *Geophysical Research Letters,* 46**,** 8046-8055.

Drouin, V., F. Sigmundsson, B. G. Ófeigsson, S. Hreinsdóttir, E. Sturkell & P. Einarsson (2017) Deformation in the Northern Volcanic Zone of Iceland 2008–2014: An interplay of tectonic, magmatic, and glacial isostatic deformation. *Journal of Geophysical Research: Solid Earth,* 122**,** 3158-3178.

Einarsson, P. (2008) Plate boundaries, rifts and transforms in Iceland. *Jökull,* 58**,** 35-38.

Geirsson, H., P. LaFemina, T. Árnadóttir, E. Sturkell, F. Sigmundsson, M. Travis, P. Schmidt, B. Lund, S. Hreinsdóttir & R. Bennett (2012) Volcano deformation at active plate

boundaries: Deep magma accumulation at Hekla volcano and plate boundary deformation in south Iceland. *Journal of Geophysical Research: Solid Earth,* 117**,** n/a-n/a.

Hreinsdóttir, S., T. Árnadóttir, J. Decriem, H. Geirsson, A. Tryggvason, R. A. Bennett & P. LaFemina (2009) A complex earthquake sequence captured by the continuous GPS network in SW Iceland. *Geophysical Research Letters,* 36.

Jónsson, S., Y. Cao, H. Vasyura-Bathke & X. Li. 2020. Surface fractures and deformation of the magnitude 5.6 earthquake near Reykjavík on 20 October 2020. In *EGU*, EGU21-12845.

Jónsson, S., P. Segall, R. Pedersen & G. Björnsson (2003) Post-earthquake ground movements correlated to pore-pressure transients. *Nature,* 424**,** 179-183.

Lauknes, T. R., H. A. Zebker & Y. Larsen (2011) InSAR Deformation Time Series Using an L_{1}-Norm Small-Baseline Approach. *IEEE Transactions on Geoscience and Remote Sensing,* 49**,** 536-546.

Li, S., F. Sigmundsson, V. Drouin, M. M. Parks, B. G. Ófeigsson, K. Jónsdóttir, R. Grapenthin, H. Geirsson, A. Hooper & S. Hreinsdóttir (2021) Ground Deformation After a Caldera Collapse: Contributions of Magma Inflow and Viscoelastic Response to the 2015–2018 Deformation Field Around Bárðarbunga, Iceland. *Journal of Geophysical Research: Solid Earth,* 126.

Li, Z. W., X. L. Ding, C. Huang, J. J. Zhu & Y. L. Chen (2008) Improved filtering parameter determination for the Goldstein radar interferogram filter. *ISPRS Journal of Photogrammetry and Remote Sensing,* 63**,** 621-634.

Metzger, S. & S. Jónsson (2014) Plate boundary deformation in North Iceland during 1992–2009 revealed by InSAR time-series analysis and GPS. *Tectonophysics,* 634**,** 127-138.

Metzger, S., S. Jónsson & H. Geirsson (2011) Locking depth and slip-rate of the Húsavík Flatey fault, North Iceland, derived from continuous GPS data 2006-2010. *Geophysical Journal International,* 187**,** 564-576.

Ofeigsson, B. G., A. Hooper, F. Sigmundsson, E. Sturkell & R. Grapenthin (2011) Deep magma storage at Hekla volcano, Iceland, revealed by InSAR time series analysis. *Journal of Geophysical Research,* 116.

Pedersen, R. (2004) InSAR based sill model links spatially offset areas of deformation and seismicity for the 1994 unrest episode at Eyjafjallajökull volcano, Iceland. *Geophysical Research Letters,* 31.

Pedersen, R. & F. Sigmundsson (2005) Temporal development of the 1999 intrusive episode in the Eyjafjallajökull volcano, Iceland, derived from InSAR images. *Bulletin of Volcanology,* 68**,** 377-393.

Pedersen, R., F. Sigmundsson & T. Masterlark (2009) Rheologic controls on inter-rifting deformation of the Northern Volcanic Zone, Iceland. *Earth and Planetary Science Letters,* 281**,** 14-26.

Schmidt, P., B. Lund & C. Hieronymus (2012) Implementation of the glacial rebound prestress advection correction in general-purpose finite element analysis software: Springs versus foundations. *Computers & Geosciences,* 40**,** 97-106.

Sigmundsson, F. 2006. *Iceland geodynamics: crustal deformation and divergent plate tectonics*. Springer Science & Business Media.

Sigmundsson, F., P. Einarsson, Á. R. Hjartardóttir, V. Drouin, K. Jónsdóttir, T. Árnadóttir, H. Geirsson, S. Hreinsdóttir, S. Li & B. G. Ófeigsson (2020) Geodynamics of Iceland and the signatures of plate spreading. *Journal of Volcanology and Geothermal Research,* 391.

Sigmundsson, F., A. Hooper, S. Hreinsdottir, K. S. Vogfjord, B. G. Ofeigsson, E. R. Heimisson, S. Dumont, M. Parks, K. Spaans, G. B. Gudmundsson, V. Drouin, T. Arnadottir, K.

Jonsdottir, M. T. Gudmundsson, T. Hognadottir, H. M. Fridriksdottir, M. Hensch, P. Einarsson, E. Magnusson, S. Samsonov, B. Brandsdottir, R. S. White, T. Agustsdottir, T. Greenfield, R. G. Green, A. R. Hjartardottir, R. Pedersen, R. A. Bennett, H. Geirsson, P. C. La Femina, H. Bjornsson, F. Palsson, E. Sturkell, C. J. Bean, M. Mollhoff, A. K. Braiden & E. P. Eibl (2015) Segmented lateral dyke growth in a rifting event at Baretharbunga volcanic system, Iceland. *Nature,* 517**,** 191-5.

Sudhaus, H. & S. Jónsson (2009) Improved source modelling through combined use of InSAR and GPS under consideration of correlated data errors: application to the June 2000 Kleifarvatn earthquake, Iceland. *Geophysical Journal International,* 176**,** 389-404.

Thordarson, T. & G. Larsen (2007) Volcanism in Iceland in historical time: Volcano types, eruption styles and eruptive history. *Journal of Geodynamics,* 43**,** 118-152.

Vadon, H. & F. Sigmundsson (1997) Crustal deformation from 1992 to 1995 at the Mid-Atlantic Ridge, southwest Iceland, mapped by satellite radar interferometry. *Science,* 275**,** 194-197.

Wegnüller, U., C. Werner, T. Strozzi, A. Wiesmann, O. Frey & M. Santoro (2016) Sentinel-1 Support in the GAMMA Software. *Procedia Computer Science,* 100**,** 1305-1312.

Werner, C., U. Wegmüller, T. Strozzi & A. Wiesmann. 2002. Processing strategies for phase unwrapping for INSAR applications. In *proceedings of the European conference on synthetic aperture radar (EUSAR 2002)*.

Wright, T. J. (2004) Toward mapping surface deformation in three dimensions using InSAR. *Geophysical Research Letters,* 31.